Earth and Planetary Science Letters 601 (2023) 117909

Contents lists available at ScienceDirect

Earth and Planetary Science Letters

journal homepage: www.elsevier.com/locate/epsl

Quartz-hosted inclusions and embayments reveal storage, fluxing, and ascent of the Mesa Falls Tuff, Yellowstone

Kenneth S. Befus [a,*], Anna C. Ruefer [a,b], Chelsea M. Allison [a], James O. Thompson [a,c]

[a] Baylor University, Department of Geosciences, Waco, TX, USA
[b] Stanford University, Department of Geological Sciences, Palo Alto, CA, USA
[c] University of Pittsburgh, Department of Geology and Environmental Science, Pittsburgh, PA, USA

ARTICLE INFO

Article history:
Received 18 August 2022
Received in revised form 30 October 2022
Accepted 5 November 2022
Available online xxxx
Editor: C.M. Petrone

Keywords:
embayments
reentrants
Yellowstone
Mesa Falls
inclusions
2D diffusion modeling

ABSTRACT

Quartz-hosted glasses from the Mesa Falls Tuff provide a geochemical window into the pre-eruptive magmatic system from one of Yellowstone's largest-volume caldera-forming eruptions. H_2O and CO_2 concentrations, along with major and trace elements, were measured in both fully enclosed glass inclusions and partially enclosed embayments in the same quartz crystals. Major elements are largely consistent between the inclusions and embayments, except for K_2O and Na_2O. Of note, K_2O is enriched by ~1 wt.% in embayment interiors relative to inclusions. Most trace elements are also enriched in the embayment interiors compared to inclusions from the same crystals. Fractionation trends of trace elements are consistent with ~30-60% crystallization. Quartz-hosted glass inclusions preserve 3.1±0.9 wt.% H_2O and 493±227 ppm CO_2 whereas embayment interiors have 0.9±0.1 wt.% H_2O and 399±229 ppm CO_2. The CO_2 is roughly similar, but the distinct ~2 wt.% discrepancy between inclusion and embayment interior H_2O contents may have been produced by CO_2 fluxing sourced from underplated Yellowstone basalts. H_2O gradients within embayments are flat in their interiors and modified by sharp positive gradients near embayment exteriors which were produced by post-eruptive rehydration. CO_2 gradients occur as gently sloping concentration gradients that extend inward 150 to 250 μm from the embayment exterior. Finite-difference 1D and 2D diffusion modeling indicates the distribution of H_2O and CO_2 in embayments was produced by slow, fluid-saturated decompression that preceded rapid ascent during the caldera-forming eruption.

1. Introduction

Magmatic processes influence the production of continental crust, generate economic ore bodies, and precede volcanic eruptions. Direct observations of these subsurface processes are impossible, and thus petrologic constraints on them rely upon datasets extracted from the crystal record. A special opportunity to constrain magmatic processes is regularly provided by igneous crystals that host small parcels of melt as embayments and inclusions. The host crystal insulates these small bodies of melt from modification during subsequent magmatic evolution and volcanic eruption. Inclusions are fully enclosed within the crystal host, and for this reason represent a geochemical proxy of the magma reservoir at the time of entrapment. Embayments, on the other hand, are fortuitously "leaky" melt pockets. The open channel allows entrapped melt within an embayment's interior to physically and geochemically react to changes in the surrounding magmatic environment. Melt in embayments and inclusions quenches to relatively inert glass during volcanic eruptions. The scientific value offered by glass inclusions to inform magmatic conditions, evolution, and pre-eruptive volatile contents is well established amongst petrologists (e.g., Lowenstern, 1995; Wallace et al., 1995). Embayments began to receive significant attention only recently after improved analytical and numerical techniques facilitated the interpretation of concentration gradients generated by diffusive re-equilibration (Anderson, 1991; Liu et al., 2007; Humphreys et al., 2008). Opportunities now exist to assess the combined petrologic record of inclusions and embayments to constrain pre-eruptive conditions and timescales of syn-eruptive processes using crystals from a single magmatic system (e.g., Myers et al., 2016, 2018; Geshi et al., 2021; Saalfeld et al., 2022).

To learn more about the behavior of a magmatic reservoir leading up to an episode of caldera-forming silicic volcanism, we compare quartz-hosted glass inclusions and embayments from Yellowstone's Mesa Falls Tuff (USA). The Mesa Falls Tuff occurs as ~280 km^3 of crystal-rich rhyolitic pyroclastic deposits erupted

* Corresponding author.
E-mail address: Kenneth_Befus@Baylor.edu (K.S. Befus).

https://doi.org/10.1016/j.epsl.2022.117909
0012-821X/

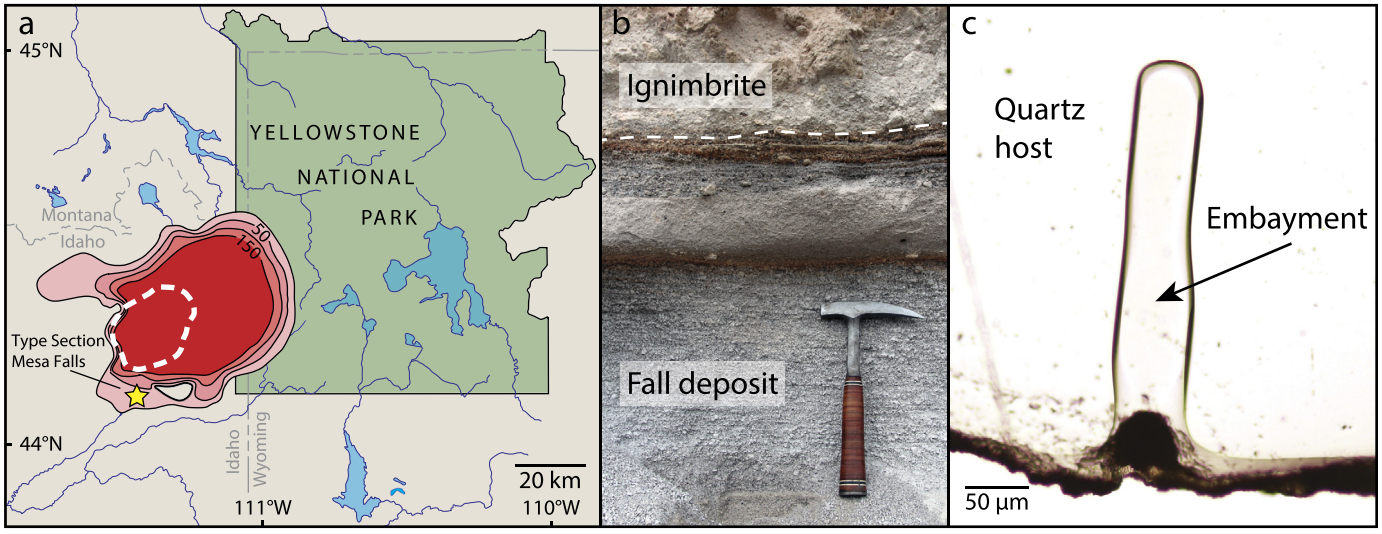

Fig. 1. a) Map of Yellowstone National Park and the mapped extent of the Mesa Falls Tuff ignimbrite sheet shown in red inferred to have erupted from Henry's Fork Caldera outlined in white dashed line. Isopach contours in m (after Christiansen, 2001). Sample collected at the Mesa Falls type section indicated by the yellow star. b) Field photo showing the outcrop of the fall deposit overlain by unwelded ignimbrite, containing large, crystal-rich pumices. Dashed line indicates the contact between ignimbrite and fall. Sample material was collected from the fall deposit near the handle of the hammer. c) Photomicrograph of a cylindrical quartz-hosted embayment (Sample MF-4). (For interpretation of the colors in the figure(s), the reader is referred to the web version of this article.)

from Henry's Fork Caldera at 1.300±0.001 Ma (Christiansen, 2001; Rivera et al., 2016; Stelten et al., 2018; Ellis et al., 2017). Euhedral quartz phenocrysts are abundant throughout the Mesa Falls Tuff deposit, and many host clear glassy inclusions and embayments. We analyzed the volatile, major, and trace element compositions of glass inclusions and embayments hosted in the same quartz crystals using high spatial resolution techniques, including synchrotron Fourier Transform Infrared spectroscopy. We used the compositions of glass inclusions compared with the record from embayments to discern details of the petrologic processes occurring in the pre-eruptive magma. Importantly, embayment interiors are depleted in H_2O relative to glass inclusions. Punctuated CO_2 flux derived from underplated basalts and the Yellowstone plume may explain this change in volatile abundance. The concentrations of H_2O and CO_2 along the length of embayments show diffusion-limited gradients, which we modeled in both one and two dimensions to assess rates of magma ascent. The estimated decompression rates are so slow that they may not recover timescales of eruptive ascent. We suggest the distribution of H_2O and CO_2 in Mesa Falls quartz instead reflects decompression of the pre-eruptive reservoir leading up to the caldera-forming eruption.

2. Materials and methods

We collected pumice clasts and loose bulk fall material from a single stratigraphic position at a Mesa Falls section off Highway 20, outside the caldera margin between Island Park and Ashton, ID (44.12204, -111.44182, Stop 1.2 in Vazquez et al., 2017) (Fig. 1a, b). At this location Mesa Falls material occurs as ∼5 m of white planar-bedded fall deposits that rest upon older unconsolidated loess and welded Huckleberry Ridge Tuff (Fig. 1b). The fall is overlain by unwelded pink Mesa Falls ignimbrite. Pumice and loose aggregate of fall material were crushed, sieved, and picked for unfractured quartz phenocrysts. Glassy embayments were identified, orientated, and doubly-polished. The quartz crystals were strong and did not shatter during grinding. Despite this advantage attrition was common. We lost >100 partially-completed specimens during grinding, polishing, and multiple analytical sessions. We did not specifically target glass inclusions, but some were fortuitously aligned in the same plane as an embayment. Our dataset thus includes 20 doubly-exposed inclusions in addition to 40 embayments.

To quantify the full crystal assemblage, we analyzed decimeter-scale unwelded pumice clasts from the unwelded ignimbrite. We crushed some pumice clasts and sliced others into flat slabs. We photographically scanned 10 pumices slabs (total area of ∼700 cm^2) and used ImageJ to measure the crystal content and modal abundance of 'mafic' and 'felsic' phases. We then established the relative abundance of specific phases in the slabs and mineral separates.

Embayment and glass inclusion H_2O and CO_2 concentrations were measured using Fourier Transform Infrared spectroscopy (FTIR). Spectra were collected using a conventional Nicolet-iN10 FTIR at Baylor University (USA), as well as the synchrotron-source infrared system on Beamline 1.4 at the Advanced Light Source at Lawrence-Berkeley National Lab (USA). At both labs we collected spectra from 500 to 7000 cm^{-1}. Absorbances at 3500 and 2350 cm^{-1} were converted to volatile concentrations of total H_2O and CO_2 using the Beer-Lambert Law and molar absorption coefficients of 71 L cm^{-1} mol^{-1} and 1214 L cm^{-1} mol^{-1}, respectively (Behrens et al., 2004; Newman et al., 1986). For 3500 cm^{-1} we choose 71 L cm^{-1} mol^{-1} as a suitable approximation for the absorption coefficient because the McIntosh et al. (2017) species-dependent approach does not significantly influence results in this study (Supplemental 1). We also measured absorption of the 1630 cm^{-1} molecular H_2O peak and converted to concentration using an absorption coefficient of 55 L cm^{-1} mol^{-1} from Newman et al. (1986) (Supplemental 1). We used 2350 g L^{-1} as a representative density for rhyolite glass. Concentrations of molecular H_2O and hydroxyl were calculated from absorbances at 5200 cm^{-1} and 4500 cm^{-1} using the model of Zhang et al. (1997). The 4500 cm^{-1} hydroxyl peak was not strong enough to quantify in most embayments. Linear baselines were subtracted from spectra to determine absorbance for each peak. Sample thicknesses were measured with the change in stage height after focusing a petrographic microscope on the top and bottom of specimen and then applying a correction for the refractive index of the glass (n∼1.5). Uncertainties in thickness range up to 6 µm. Because thickness is likely the greatest source of uncertainty in FTIR analyses, we use the standard deviation of sample thickness to establish error bars for our volatile data.

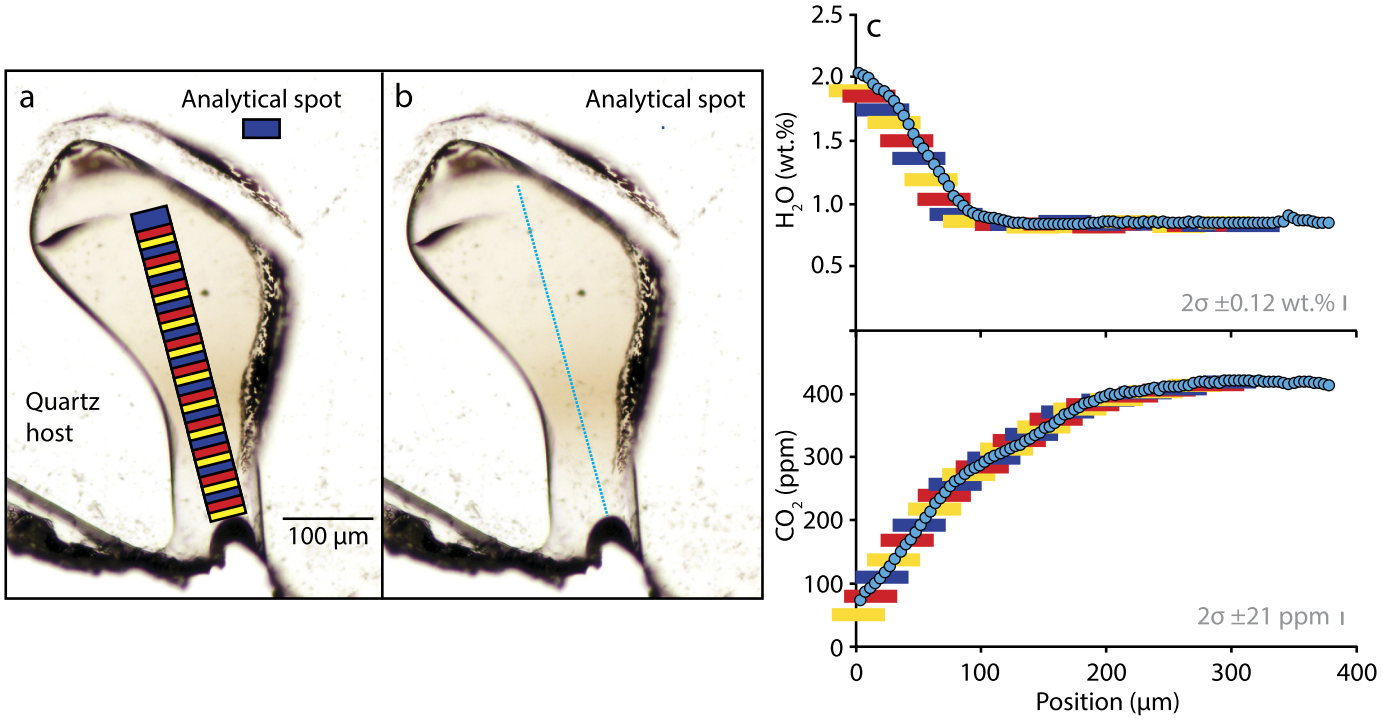

Fig. 2. Demonstration of the spatial resolution of a) conventional FTIR with a 40 × 20 µm aperture overlapping 10 µm steps and b) synchrotron FTIR with a 3 µm diffraction-limited spot size and 4 µm steps, applied to embayment MF-35. c) and d) the influence of spatial resolution on concentration gradients of H_2O and CO_2, respectively. Position marks increasing distance into the host crystal, meaning 0 µm is the exterior margin of the embayment glass. In MF-35 the techniques reproduce excellently, but in others the larger analytical spot returns lower values. The curved crack 'above' the embayment in panels a and b formed during sample preparation. It demonstrates embayments affect the distribution of residual stresses in quartz.

All embayments were analyzed using synchrotron FTIR. The exceptional brightness of the synchrotron light source allowed us to collect spectra with 4 to 16 scans at 4 cm^{-1} spectral resolution, with a ~3 µm diffraction-limited spot size. We collected linear transects across all embayments with 2 or 4 µm step. We also collected 2D maps for 15 embayments with a 4 or 5 µm step. Transects were also collected along embayments with 16 to 64 scans at 4 cm^{-1} spectral resolution using conventional FTIR. Most apertures were squares (ranged from 20 × 20 µm to 40 × 40 µm), but some were rectangular (20 × 40 µm) to best optimize signal. The step size between individual analyses was 10 µm so consecutive analyses overlapped (Fig. 2). Conventional FTIR produced similar volatile gradients to the synchrotron, although it sometimes yielded lower contents, likely as a result of the wider aperture. The high spatial resolution of synchrotron data lends more confidence to our analysis of H_2O and CO_2 distributions and thus remains the focus here. Volatile concentrations of glass inclusions were measured at conventional spatial resolution on the Nicolet-iN10 FTIR. For glass inclusions each spectrum consisted of 64 scans at 4 cm^{-1} spectral resolution using a 40 × 40 µm aperture centered within the inclusions.

Major and trace element compositions were collected for all glass inclusions, matrix glasses, and embayments. Embayments were analyzed at the interior of the embayment glass, i.e., the part of the embayment deepest inside the quartz crystal. Some longer embayments were also analyzed at a position on the glass close to the edge of the quartz crystal, i.e., the "exterior" of the embayment. Some embayments were analyzed with a scan across their full length (from the interior to exterior), and those scans were performed prior to any spot analyses on the sample.

Trace element compositions of the glasses were analyzed by laser ablation inductively coupled plasma mass spectrometry (LA-ICP-MS) at the University of Texas at Austin using a New Wave UP 193-FX excimer laser coupled with an Agilent 7500ce spectrometer. Analytical conditions were selected after careful optimization and tuning on NIST 612 and embayment glass. All samples were pre-ablated prior to analysis. Spot analyses were conducted using a 50 µm diameter aperture. Spot analyses used a 45 s dwell time, 20 Hz laser repeat rate, and 55% beam energy, corresponding to ~4 J cm^{-2} fluence. The scans across select embayments were conducted using a 35 µm diameter aperture at a scan rate of 5 µm s^{-1}, 20 Hz laser repeat rate, and 55% beam energy, yielding ~4 J cm^{-2} fluence. Scanning conditions and the system's washout of <1 s produced a spatial resolution of ~3.3 µm. NIST 612 was used as the primary calibration standard, with NIST 610 as a secondary standard. The standard glasses were analyzed multiple times during the session to check for instrument drift. Trace element concentrations were calculated with ^{29}Si as the internal standard using the Iolite 4 data processing software, and assuming 75 wt.% SiO_2 in the glasses.

Major elements were analyzed using the Cameca SX Five electron microprobe at Texas A&M University. We chose analytical spots near LA-ICP-MS ablation pits for all samples so positions are comparable. All microprobe analyses were conducted using 10 nA beam current with 15 KeV accelerating voltage and a defocused 10 µm diameter beam. Elements were counted for 20 s on peak and 10 s on background, with Na measured first in the sequence. The microprobe was calibrated using mineral standards, with a Yellowstone rhyolite glass secondary standard analyzed periodically throughout the session (Smithsonian Standard VG 568).

We developed a diffusion model to explore the 1D (linear) and 2D (maps) distribution of H_2O and CO_2 in embayments. Volatile diffusion is modeled in response to constant decompression in an isothermal closed system. We use finite-difference numerical modeling to solve the diffusion equation in 1D or 2D:

$$C_i^{n+1} = C_i^n + D\Delta t\left(\frac{C_{i+1}^n - 2C_i^n + C_{i-1}^n}{\Delta x}\right) \quad (1)$$

$$C_{i,j}^{n+1} = C_{i,j}^{n} + D\Delta t\left(\frac{C_{i+1,j}^{n} - 2C_{i,j}^{n} + C_{i-1,j}^{n}}{(\Delta x)^2} + \frac{C_{i,j+1}^{n} - 2C_{i,j}^{n} + C_{i,j-j}^{n}}{(\Delta y)^2}\right) \quad (2)$$

where D is the diffusion coefficient, C is the volatile concentration, Δt is the time interval, Δx and Δy are the discrete distances. The diffusion coefficient for H_2O in rhyolite glass is calculated from Ni and Zhang (2008) and Zhang and Ni (2010) for concentrations less than and greater than 2 wt.%, respectively. Diffusivity for CO_2 is derived from Zhang and Ni (2010). To create an infinite sink for volatiles outside the embayment we assume the diffusivity of both volatiles is an order of magnitude faster in the exterior melt than in embayment melt. We handle the crystal-glass boundary by setting diffusion orders of magnitude slower in the host crystal than melt. Volatile solubility in the melt follows closed-system degassing paths using Liu et al. (2005). Initially, all melt has a uniform concentration based on user input starting conditions and may include an exsolved vapor phase. At each timestep during decompression the mole fraction of exsolved and dissolved H_2O and CO_2 in the exterior melt update and balance. That change in the exterior melt's exsolved and dissolved volatiles creates the disequilibrium that produces diffusion-limited concentration gradients in the model embayment. The model uses a convergence gradual declining fit search of parameter space to find the best match to the data. Specifically, the model calculates the root mean squares between the model and data at each iteration, with the lowest value representing the best match. Upon convergence to the lowest root mean squares, the model finishes computation and presents best fit parameters. It also produces a visual overlay of the model results on instrument data. Solutions from 1D and 2D models for the same embayment return comparable results. Differences between the solutions to the 1D and 2D models are caused by user decisions, 1D linear transects relative to 2D embayment geometry (e.g., deGraffenried and Shea, 2021), and input instrument data. We acknowledge that modeling processes in a complex magmatic system introduces complications as a result of necessary assumptions (e.g., Brugman et al., 2022). We benchmarked our models against EMBER, an important open-source model recently provided to the petrologic community (Georgeais et al., 2021). Our model returns best-fit CO_2 profiles within 3% of EMBER (2σ). The decompression rate and quench pressure varied by <10% (<0.00025 MPa s^{-1}) and <35% (<12 MPa), respectively. Discrepancies arise because the models rely on different mechanisms to define the initial and final conditions and find the best fit to the instrument data. Our model and its user manual are provided in Supplemental 5 and at Github.com (https://github.com/jthompson2710/Embayment_Diffuser).

3. Results

The Mesa Falls Tuff is crystal rich, containing an assemblage of quartz, sanidine (~Or_{60}), plagioclase (~An_{15}), clinopyroxene, orthopyroxene, fayalite, magnetite, ilmenite, zircon, fluorapatite, and chevkinite (e.g., Christiansen, 2001; Neukampf et al., 2019). Our counts indicate crystals occupy 7% to 10% of pumice slabs, which scales to 25±5% dense rock equivalent in agreement with Neace et al. (1986). Sanidine and quartz account for 95 to 99% of the total crystal population, with those phases being in near equal proportion. Plagioclase is rare, making up <1% of the mineral assemblage, and most commonly occurs in contact with mafic phases. Fe-Ti oxides, clinopyroxene, and fayalite are the common 'mafic' phases, occurring at ~1%, 0.5% and 0.3%, respectively. Orthopyroxene is rarer than other mafic phases, and most commonly exists as cores in clinopyroxene. Together the mafic phases account for ~2% of the total crystal population. We also identified zircon, fluorapatite, and chevkinite as rare accessory phases (<0.1%).

Quartz crystals are typically unfractured euhedral bipyramids, which occur up to 4 mm in size in our samples. Embayments are present in ~50% of Mesa Falls quartz (Ruefer et al., 2021). Only straight tubes and thick-bulbed embayment forms survived sample preparation, and in roughly equal proportions. The successfully-prepared embayments range in length from 190 to 670 µm (Table 1). Straight tube, cylindrical embayments were 50 to 180 µm in diameter. Bulbed embayments had thinner necks near the embayment opening (40 to 200 µm across) compared with the bulbed interiors (100 to 260 µm across). All of the selected embayments were filled with dense, clear rhyolite glass. No bubbles occurred within the embayment interiors. A concave bubble wall occurred at the exterior mouth in 34 of the embayments. In the remaining 6 we define the exterior boundary using the crystal faces of the host quartz.

Embayment glasses preserve consistent H_2O concentrations across much of their interiors (Fig. 3a). Within individual embayments the interior H_2O concentrations range from 0.8±0.1 to 1.1±0.1 wt.%, and average 0.9±0.1 wt.% across the full population (Table 1, 2σ). Water speciation is roughly equally distributed between molecular H_2O and hydroxyl in embayment interiors (Supplemental 1). Consistent interior H_2O contents abruptly transform into steep H_2O concentration gradients near embayment exteriors. Enrichments of H_2O in the gradients increase from the inner plateau values to contents of 1.7±0.1 to 2.8±0.1 wt.%, averaging 2.1±0.5 wt.%. As opposed to the embayment interiors where there is abundant hydroxyl, molecular H_2O accounts for the majority of the H_2O in the exterior enrichments (Supplemental 1). The H_2O enrichments above plateau values extend only ~100 µm (50 to 135 µm) into the embayment interiors. All of the embayments preserve CO_2 along diffusion-equilibrated concentration gradients (Fig. 3b). CO_2 contents in the embayment interiors range from 81±5 to 558±45 ppm, and as a group average 399±229 ppm (Table 1, 2σ). CO_2 concentrations are relatively flat and consistent across the interiors of individual embayments. These plateaus of CO_2 begin to decrease along gradients around 150 to 250 µm from the embayment exterior. At the embayment exterior the median CO_2 content is 108 ppm, with the full range 22±2 to 237±5 ppm. Those CO_2 contents suggest final saturation pressures ranging from 10 to 43 MPa, and average 21±15 MPa (Supplemental 4, 2σ).

We also analyzed 20 fully entrapped glass inclusions from Mesa Falls that occur within the same host quartz crystals as the embayments (Supplemental 2). The analyzed glass inclusions primarily occurred as faceted, roughly equant parallelograms that ranged from 70 to 200 µm across. Each contained clear rhyolite glass. Those with a rare bubble ~5 µm across preserved indistinguishable volatile contents compared to the full population. The 20 glass inclusions in our study contain 3.1±0.9 wt.% H_2O and 493±227 ppm CO_2 (2σ, Fig. 4). These H_2O contents are similar to values reported by Tollan et al. (2019) for unexposed inclusions, however our CO_2 concentrations tend to be greater by ~100 ppm. Volatile contents indicate entrapment pressures of 100 to 175 MPa and mole fractions of 50±15% CO_2 to 50±15% H_2O assuming fluid saturation using Liu et al. (2007). The CO_2 contents in the glass inclusions are equivalent to or slightly greater than those preserved in the embayment interiors, whereas H_2O content is significantly higher in inclusions (>2 wt.%).

Quartz-hosted glass inclusions, embayments, and matrix glasses are rhyolite with 72 to 76 wt.% SiO_2 (Table 2, Supplemental 2). Major element concentrations are indistinguishable between each sample type except in alkalis. K_2O concentrations in embayment interiors are 6.0±0.3 wt.%, which is ~1 wt.% greater than in glass inclusions (5.1±0.2) (Fig. 5a). Na_2O preserves a subtle correlation in the opposite direction; inclusions are enriched by 0.3 wt.%

Table 1
Volatile contents and shape of the embayments. Italicized values are 2σ uncertainties for each calculated value. H_2O_{mol} was measured from absorption at 5200 cm^{-1}. "-" represents data below detection. Full transects are provided in Supplemental 1.

Interior volatiles							Exterior volatiles								Shape descriptions		
Embayment	H_2O_{3500} (wt.%)		H_2O_{mol} (wt.%)		CO_2 (ppm)		H_2O_{3500} (wt.%)		H_2O_{mol} (wt.%)		H_2O inflexion (μm)		CO_2 (ppm)		Form	Length (μm)	Diameter (μm)
MF-1	0.8	*0.1*	0.2	*0.1*	456	*28*	2.0	*0.2*	1.9	*0.2*	62	*4*	140	*11*	Straight	400	80
MF-2	0.8	*0.1*	0.3	*0.1*	302	*18*	2.2	*0.1*	2.3	*0.1*	67	*3*	117	*12*	Bulb	290	50 to 100
MF-4	0.9	*0.1*	0.2	*0.1*	437	*11*	2.4	*0.1*	1.7	*0.1*	93	*3*	185	*8*	Straight	420	50
MF-5b	1.0	*0.1*	-	-	510	*8*	2.0	*0.1*	-	-	82	*4*	237	*5*	Bulb	230	80 to 130
MF-6	0.9	*0.1*	0.2	*0.1*	425	*12*	1.7	*0.1*	1.7	*0.1*	96	*4*	67	*6*	Bulb	250	80 to 150
MF-8	1.1	*0.1*	0.4	*0.1*	122	*11*	2.4	*0.3*	2.0	*0.3*	95	*3*	42	*6*	Straight	200	110
MF-9	0.9	*0.1*	0.3	*0.1*	370	*35*	2.4	*0.3*	1.6	*0.3*	84	*4*	136	*16*	Bulb	280	70 to 140
MF-10	0.9	*0.1*	0.2	*0.1*	463	*52*	2.3	*0.1*	2.0	*0.1*	99	*3*	150	*18*	Bulb	530	100 to 150
MF-11	0.9	*0.1*	0.3	*0.1*	81	*5*	2.1	*0.1*	1.9	*0.1*	63	*3*	22	*2*	Straight	220	80
MF-12	1.0	*0.1*	0.4	*0.1*	394	*14*	2.1	*0.1*	1.9	*0.1*	58	*4*	140	*4*	Straight	190	100
MF-13	1.0	*0.1*	-	-	558	*45*	1.8	*0.3*	-	-	53	*3*	125	*30*	Bulb	400	40 to 170
MF-14	0.9	*0.1*	0.1	*0.1*	418	*52*	2.8	*0.1*	2.5	*0.1*	80	*4*	91	*60*	Bulb	390	90 to 120
MF-15	0.9	*0.1*	0.3	*0.1*	480	*25*	2.3	*0.1*	1.8	*0.1*	78	*4*	78	*6*	Straight	300	150
MF-16	1.0	*0.1*	0.3	*0.1*	362	*10*	2.1	*0.1*	1.8	*0.1*	118	*4*	110	*5*	Bulb	240	100 to 160
MF-17	1.0	*0.1*	0.3	*0.1*	487	*17*	2.3	*0.1*	2.0	*0.1*	77	*3*	176	*9*	Straight	320	100
MF-18	0.8	*0.1*	0.2	*0.1*	458	*29*	2.2	*0.2*	1.7	*0.2*	93	*5*	119	*12*	Bulb	610	90 to 210
MF-19	0.9	*0.1*	0.3	*0.1*	457	*22*	1.6	*0.1*	1.5	*0.1*	67	*5*	198	*12*	Straight	200	120
MF-20	0.9	*0.1*	0.3	*0.1*	452	*41*	2.3	*0.3*	2.0	*0.3*	82	*4*	89	*17*	Bulb	400	100 to 200
MF-21	0.9	*0.1*	0.2	*0.1*	540	*29*	1.7	*0.3*	1.5	*0.3*	59	*5*	146	*12*	Bulb	400	90 to 200
MF-22	0.9	*0.1*	0.3	*0.1*	431	*15*	1.9	*0.1*	1.6	*0.1*	76	*4*	173	*8*	Bulb	250	70 to 100
MF-25	1.0	*0.1*	0.4	*0.1*	459	*62*	2.2	*0.3*	1.7	*0.3*	80	*4*	93	*12*	Bulb	500	70 to 110
MF-27	0.9	*0.1*	0.1	*0.1*	545	*12*	2.5	*0.1*	2.1	*0.1*	135	*5*	105	*3*	Straight	670	160
MF-28	0.9	*0.1*	0.1	*0.1*	519	*55*	2.3	*0.2*	2.0	*0.2*	92	*4*	94	*7*	Bulb	500	100 to 170
MF-29	1.0	*0.1*	0.3	*0.1*	255	*21*	2.4	*0.3*	2.1	*0.3*	80	*4*	92	*10*	Straight	190	100
MF-30	0.9	*0.1*	0.2	*0.1*	362	*15*	1.7	*0.1*	1.3	*0.1*	64	*8*	114	*6*	Bulb	350	120 to 220
MF-31	0.9	*0.1*	0.2	*0.1*	388	*15*	2.0	*0.1*	1.7	*0.1*	92	*4*	144	*6*	Straight	270	120
MF-32	1.0	*0.1*	0.3	*0.1*	143	*12*	2.3	*0.2*	1.9	*0.2*	118	*6*	42	*4*	Bulb	220	70 to 110
MF-33a	1.0	*0.1*	0.3	*0.1*	420	*22*	2.2	*0.2*	1.9	*0.2*	60	*4*	52	*3*	Straight	240	100
MF-33b	1.0	*0.1*	0.2	*0.1*	432	*27*	2.3	*0.2*	2.3	*0.2*	64	*4*	49	*5*	Straight	210	120
MF-35	0.8	*0.1*	0.1	*0.1*	418	*35*	2.0	*0.2*	1.8	*0.2*	96	*4*	88	*7*	Bulb	440	70 to 140
MF-36	0.9	*0.1*	0.2	*0.1*	427	*52*	2.2	*0.4*	1.6	*0.4*	88	*4*	120	*5*	Bulb	280	80 to 190
MF-37	0.8	*0.1*	0.2	*0.1*	308	*24*	2.0	*0.3*	1.7	*0.3*	94	*6*	64	*29*	Bulb	330	60 to 120
MF-39	0.9	*0.1*	0.3	*0.1*	291	*21*	2.1	*0.2*	1.9	*0.2*	108	*4*	86	*6*	Bulb	200	200 to 260
MF-40	0.9	*0.1*	0.2	*0.1*	530	*26*	2.2	*0.2*	2.0	*0.2*	112	*4*	126	*7*	Straight	600	100
MF-42	0.9	*0.1*	0.4	*0.1*	486	*17*	2.2	*0.1*	2.3	*0.1*	124	*4*	127	*8*	Straight	290	180
MF-44	0.9	*0.1*	0.3	*0.1*	361	*20*	2.2	*0.2*	2.2	*0.2*	112	*4*	43	*5*	Bulb	270	100 to 140
MF-45	0.9	*0.1*	0.4	*0.1*	241	*16*	2.1	*0.2*	2.1	*0.2*	102	*6*	59	*8*	Straight	190	130
MF-46	1.0	*0.1*	0.3	*0.1*	277	*21*	2.3	*0.2*	1.8	*0.2*	72	*4*	72	*6*	Straight	430	100
MF-48	0.9	*0.1*	0.2	*0.1*	390	*37*	1.9	*0.3*	1.8	*0.3*	56	*4*	77	*13*	Bulb	370	40 to 100
MF-50	0.8	*0.1*	0.2	*0.1*	508	*30*	2.2	*0.2*	1.7	*0.2*	72	*4*	143	*12*	Straight	480	150
Average (n=40)	0.9	*0.1*	0.2	*0.2*	399	*229*	2.1	*0.5*	1.9	*0.5*	85	*41*	108	*95*		338 *257*	

Na_2O relative to embayment interiors. We choose to report and plot compositional data as measured, rather than normalized anhydrous, because volatile concentrations are our primary objective and totals sum to near 100% (Table 2, Supplemental 2). This choice does not affect interpretations as trends and data points shift little.

Trace elements provide an additional opportunity to compare inclusions and embayment glasses, and assess their compatibility behavior with respect to the Mesa Falls mineral phase assemblage (Supplemental 2). Ba, Sr, and Eu are strongly compatible in the abundant sanidine. We use Harker-style variation diagrams to assess the compatibility of other trace elements in the glass inclusions. Most trace elements display trends in the glass inclusions. Compatible Ba correlates negatively with Rb, consistent with incompatible behavior for Rb during fractional crystallization (Fig. 5b). By iteratively plotting Ba or Rb against the other trace elements we established the relative compatibility of each element. Rb, Cs, Th, and U are the only incompatible elements. Some trace elements only produce irregular clusters and produce no clear trends. The majority of the remaining trace elements, which include rare earth and transition metals, behave as compatible elements during the episode of inclusion formation (Fig. 5c). Textural observations of glass inclusions reconcile some complexities in the trends. Most glass inclusions are partially or completely faceted (i.e., parallelograms), however three display no faceting (samples MF-5-1, MF-5-2, MF-43). Those rounded inclusions form a subpopulation with slightly higher compatible trace element concentrations, and may be younger than the faceted crystals although we cannot establish it firmly with crystal position (Pamukcu et al., 2015). Rounded inclusions sometimes plot along a similar trend as the faceted inclusions and only extend values to a higher range (Fig. 5c), but in other instances plot along their own trajectory. Similar trends appear in the Mesa Falls glass inclusion data from Neukampf et al. (2019), although the physical characteristics of those inclusions were not specified.

Trace element compositions of Mesa Falls embayment interiors display less variability than glass inclusions, despite a sample suite twice as large (Fig. 5). Concentrations tend to cluster rather than form arrays on variation diagrams. The trace element concentrations of the embayment interiors may partially or completely overlap the compositional range of the glass inclusions. When they overlap, the embayment interiors commonly occupy the higher concentration range of the glass inclusions (Fig. 5). The few exceptions are Sc, Rb, Cs, Th, and U. For those elements, embayments interiors overlap with glass inclusions without any clustering to the high end of the range. Finally, linear laser ablation scans from embayment interiors to matrix are relatively uniform for all trace elements (Fig. 6).

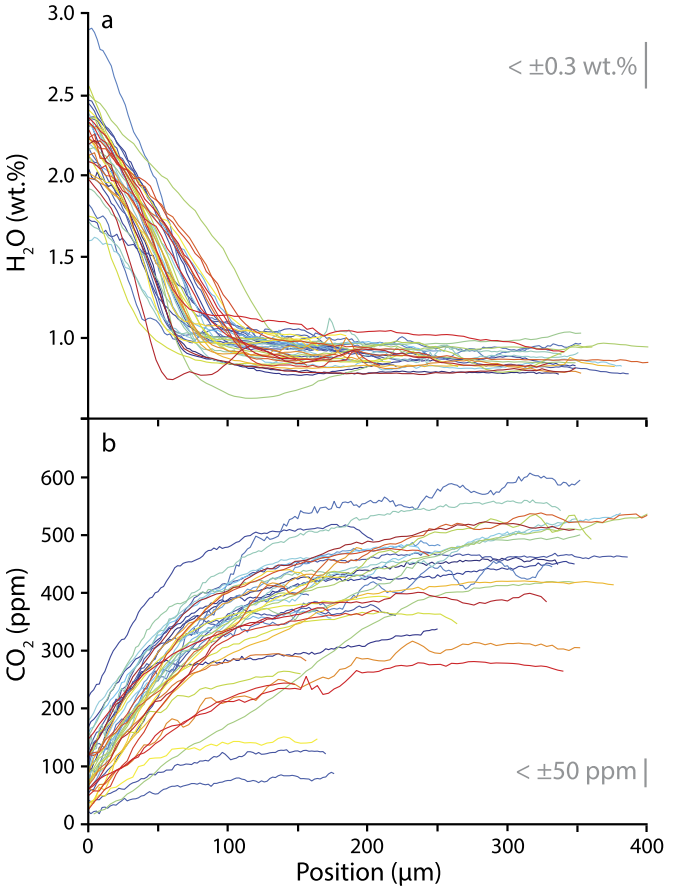

Fig. 3. Compilation of all of the H_2O and CO_2 concentration gradients measured by synchrotron FTIR. Line colors are arbitrary. As in Fig. 2, position marks increasing distance into the host crystal. The max 2σ uncertainty is less than the gray number and bar.

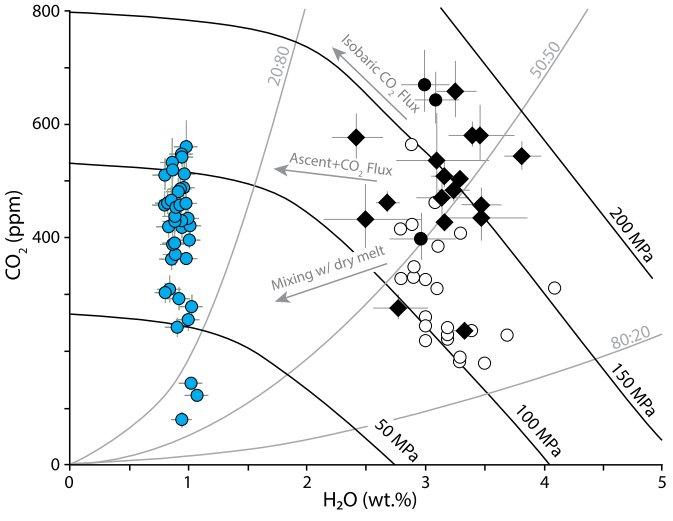

Fig. 4. Dissolved volatiles in quartz-hosted embayments (blue; representative interior contents) and glass inclusions (black diamonds except the 3 rounded inclusions shown as circles). Inclusions from Tollan et al. (2019) in white. Error bars (2σ) are shown in gray when larger than the symbol size. Equilibrium solubility at 50, 100, 150, and 200 MPa and 800 °C are shown in black. Gray curved lines are fluid compositions in percent H_2O and CO_2 for rhyolite in equilibrium with a mixed fluid (Liu et al., 2005). Gray arrows show trajectory of a fluid in response to mixing, CO_2 flux, ascent, and combinations thereof.

Table 2
Compositions of matrix glass and glass inclusions. Major elements analyzed by electron microprobe and trace elements by LA-ICP-MS. Major oxides reported in weight percent and trace elements in ppm, and both are averages of n samples. Values in parentheses represent 2σ standard deviation. See Supplemental 2 for the full dataset.

Phase		Major Elements and Volatiles													
		SiO_2	TiO_2	Al_2O_3	FeO[a]	MgO	MnO	CaO	K_2O	Na_2O	H_2O (wt.%)	CO_2 (ppm)	Total	n
Glass Inclusions	Average	73.04 (1.01)	0.11 (0.05)	11.53 (0.42)	1.09 (0.28)	0.03 (0.03)	0.03 (0.03)	0.50 (0.25)	5.08 (0.21)	3.35 (0.22)	3.11 (0.88)	493 (227)	97.84 (1.40)	20
	Max	73.84	0.14	11.96	1.28	0.06	0.05	0.92	5.26	3.52	3.82	669	99.05	
	Min	72.35	0.05	11.20	0.89	0.00	0.00	0.44	4.49	3.14	3.14	235	96.86	
Embayment interior	Average	74.41 (1.70)	0.11 (0.07)	11.80 (0.52)	1.27 (0.11)	0.03 (0.02)	0.03 (0.04)	0.51 (0.05)	6.03 (0.26)	3.04 (0.26)	0.91 (0.14)	399 (229)	98.12 (1.78)	44
	Max	76.03	0.20	12.36	1.37	0.05	0.08	0.54	6.29	3.34	1.06	558	99.61	
	Min	72.86	0.01	11.16	1.17	0.01	0.00	0.45	5.73	2.81	0.74	81	96.31	

		Select Trace Elements												
		Sc	Rb	Sr	Y	Zr	Nb	Cs	Ba	La	Ce	Th	U	n
Glass Inclusions	Average	5 (1)	232 (52)	4 (7)	55 (18)	158 (63)	48 (10)	5 (2)	58 (150)	70 (31)	138 (59)	33 (6)	8 (2)	19
	Max	6	284	14	81	231	55	7	307	102	201	40	10	
	Min	4	188	1	41	125	39	3	4	52	107	28	6	
Embayment interior	Average	5 (1)	236 (42)	7 (3)	68 (16)	172 (18)	55 (4)	5 (4)	104 (54)	78 (7)	154 (15)	33 (4)	8 (2)	41
	Max	7	317	9	88	183	62	14	129	85	169	38	10	
	Min	4	199	1	58	145	51	3	11	66	131	29	7	

[a] Total iron reported as FeO.

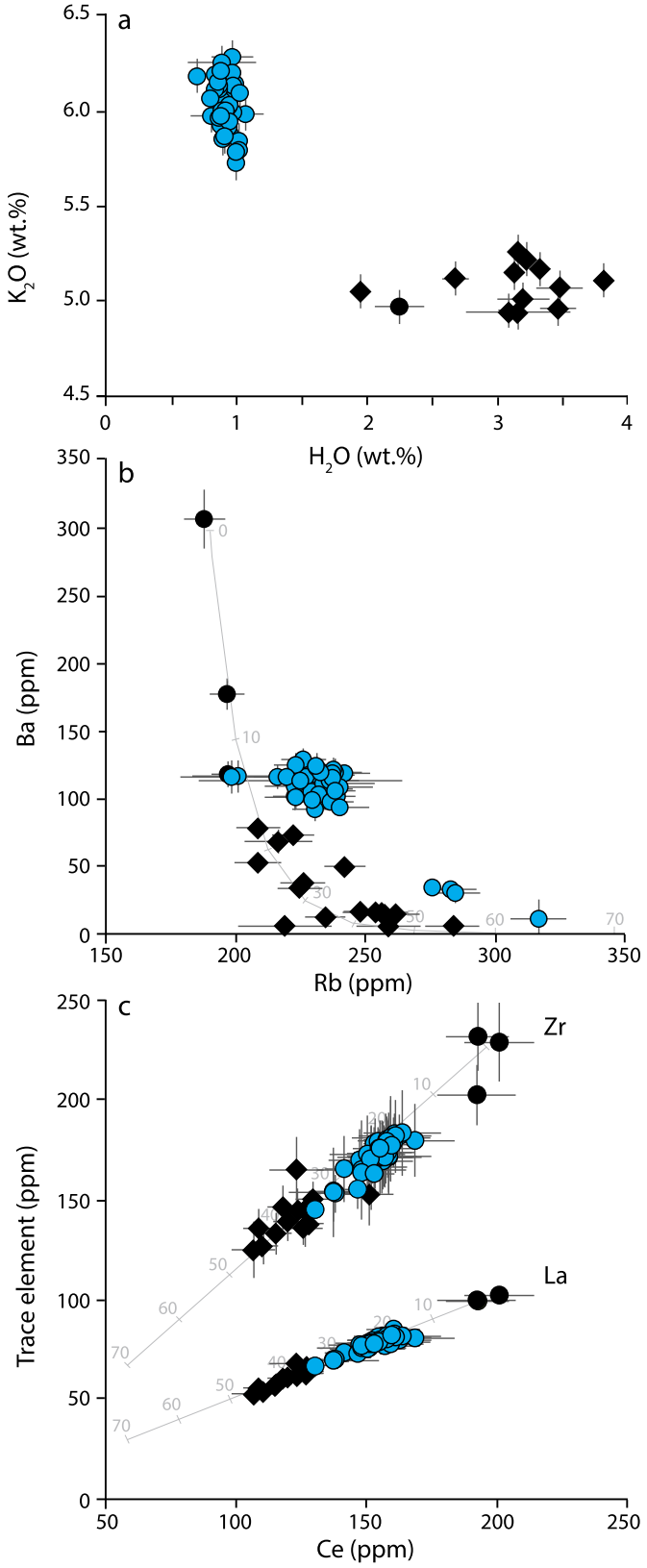

Fig. 5. Concentrations of a) major and b, c) trace elements in the embayment interiors (blue) and glass inclusions (black diamonds except the 3 rounded inclusions shown as circles). Error bars (2σ) are shown in gray when larger than the symbol size. Gray lines are Rayleigh fractionation models; tick marks represent 10% intervals of fractional crystallization.

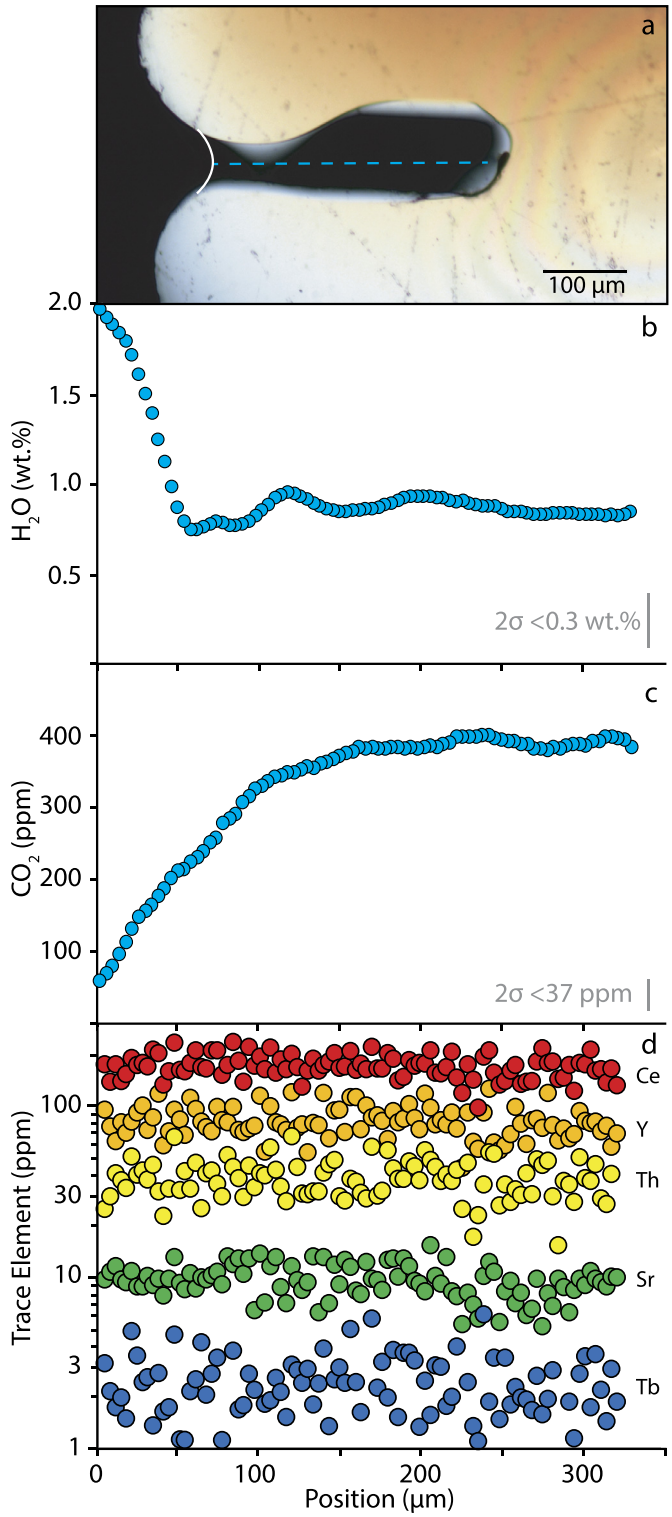

Fig. 6. a) Photomicrograph of embayment MF-48 in cross polars. Transect of synchrotron FTIR and LA-ICP-MS shown by dashed blue line extending from exterior (white line). Panels b), c), and d) show the distribution of H_2O, CO_2, and trace elements across the length of the embayment. Trace elements do not show gradients. As in Fig. 2, position marks increasing distance into the host crystal. Error bars are smaller than the symbol size for the trace elements. Gray numbers and bar indicate 2σ uncertainty for the volatiles.

4. Discussion

4.1. Petrologic insights to the Mesa Falls reservoir

Using the major element composition of quartz-hosted glass inclusions, the rhyolite-MELTS model best replicates the Mesa Falls phase assemblage and abundances at storage conditions between 750 to 800 °C and 130 to 200 MPa (5 to 8 km, assuming average crustal density of 2600 kg m^{-3}) (Gualda et al., 2012). This is similar to, or slightly cooler, than previously published Mesa Falls Tuff and Mesa Falls Tuff-related mineral-based thermometer estimates ranging from 750 to 850 °C (Rivera et al., 2016; Troch et al., 2018; Tollan et al., 2019). Assuming volatile saturation at depth, the glass inclusions indicate the magma was in equilibrium with a fluid composed of ~60 mol% CO_2 and were stored between 100 to 170 MPa (4 to 7 km, assuming average crustal density of 2600 kg m^{-3}) (Fig. 4) (Liu et al., 2007). These storage conditions are consistent with constraints from mineral compositions and experiments performed on other Yellowstone rhyolites (e.g., Christiansen, 2001; Stelten et al., 2015; Befus and Gardner, 2016; Myers et al., 2016). The Mesa Falls system differs in that it is particularly crystal-rich compared to many other Yellowstone products, with sanidine and quartz accounting for 25±5 vol.%. It is also volumetrically an outlier as one of the 'big three', infamous Yellowstone caldera-forming eruptions, although of those it is by far the smallest at ~280 km^3 (Christiansen, 2001). Together, the similarities and differences demonstrate the Mesa Falls Tuff is a distinct episode that informs both the past magmatic history and future eruptive potential of the Yellowstone caldera. Most notably, inclusions and embayments have strikingly different H_2O contents but they share a similar range of CO_2. We demonstrate that embayments and glass inclusions instead likely capture processes in the pre-eruptive Mesa Falls reservoir.

The glass inclusions preserve a record of fractional crystallization in the Mesa Falls reservoir prior to the formation of embayments. To estimate the extent of fractional crystallization we use the Rayleigh fractional crystallization model: $\frac{C_m}{C_p} = f^{(D-1)}$ where C_m is the trace element concentration in the melt inclusion, C_p is the most primitive concentration, f is the mass fraction of melt remaining (1-f is percent crystallization), and D is the bulk distribution coefficient. We recognize that the Rayleigh fractionation is a simple approximation of the natural system, but we use it here to constrain which phases crystallized during the episode of glass inclusion formation. Trace element concentrations in the glass inclusions track crystallization because bulk distribution coefficients control the slope of trends on Harker-style variation diagrams. We found the best-fit slope for data from pairs of trace elements to establish their relative bulk distribution coefficients, and define the modal abundances following published partition coefficients for each mineral (Supplemental 3). The glass inclusions reveal the crystallization history of the Mesa Falls reservoir closely aligns with petrographic observations. Our estimates indicate sanidine accounts for ~40% of the crystallizing assemblage, with quartz in similar abundance. Ba, Sr, and Eu are therefore the most compatible elements, and Rb, Cs, Th, and U are incompatible. The other rare earth and transition elements are compatible and have similar bulk distribution coefficients of ~2. Such similarity is best explained by crystallization of ~0.001% chevkinite, ~0.1% zircon, ~0.4% fluorapatite, and ~1% clinopyroxene. Bulk distribution coefficients indicate ~1% each of fayalite and magnetite. Using the Mesa Falls mineral assemblage, estimated bulk distribution coefficients, and the full suite of trace elements, fractionation estimates range from 35 to 66 wt.%, and average 50±7 wt.% during the episode of glass inclusion formation. The average for the faceted inclusion population alone drops to 44±10 wt.% crystallization. These crystallization estimates are similar to previously published estimates ranging from ~30 to ~50 wt.% for other Yellowstone magmas (e.g., Vazquez and Reid, 2002; Leeman and Phelps, 1981; Bindeman and Valley, 2001; Watts et al., 2012; Befus and Gardner, 2016; Myers et al., 2018).

4.2. Evidence for CO_2 flux

The compositions of embayment glasses record a perturbation in the Mesa Falls reservoir. When compared with inclusions, the embayment glasses are enriched in K_2O, Ba, and most compatible trace elements (Fig. 5). The distributions of most trace elements in embayment interiors are clustered and cover a more limited compositional range than the glass inclusions. Differences in H_2O between embayments and inclusions are even more pronounced (Figs. 4, 5). Inclusions hold 3.1±0.9 wt.% H_2O whereas embayment interiors have 0.9±0.1 wt.% H_2O. CO_2 contents are largely similar. Importantly, this volatile data allows us to eliminate a number of magmatic processes in the pre-eruptive reservoir (Fig. 4). Open system degassing would reduce CO_2 but maintain H_2O, opposite to what we observe. Closed-system degassing, even buffered by an exsolved fluid phase, is equally unviable because degassing paths only reach 1 wt.% H_2O at very low CO_2 contents (<50 ppm). We also discard the influence of post-entrapment crystallization of quartz host modifying the composition of the glass inclusions because we do not observe the expected modification of increasing major element concentrations in the inclusion glass. We recognize that the compositional shift recorded in the Mesa Falls embayments may have been produced by melting, mixing with a CO_2-rich rhyolite melt, infiltration by CO_2 fluid, or combinations thereof (both with or without magmatic ascent). Although alternatives exist, we propose that CO_2 fluid flux was the key mechanism.

CO_2 fluxing, or flushing, is often called upon to explain volatile abundances in mafic and silicic reservoirs (e.g., Anderson et al., 1989; Bachmann et al., 2010; Waelkens et al., 2022; Pappalardo et al., 2022). CO_2 flux represents the introduction of an external, exsolved CO_2-rich fluid to a magma reservoir (e.g., Blundy et al., 2010; Edmonds and Woods, 2018). This interaction may significantly change reservoir properties such as temperature, buoyancy, and compressibility. Importantly, exchange during CO_2 fluxing increases the partial pressure of CO_2 and consequently increases the molar fraction of CO_2 dissolved in the melt. Dissolved H_2O is reduced, which in turn will promote crystallization (e.g., Spilliaert et al., 2006). If this volatile exchange occurs at equilibrium, then the H_2O and CO_2 abundances follow solubility and supply (Fig. 4). The exsolved H_2O produces a bubbly, buoyant, and compressible melt. If equilibrium exchange was maintained during CO_2 flux in the Mesa Falls reservoir, then the shift from inclusion to embayment within a single crystal records non-eruptive decompression, perhaps facilitated by buoyancy, imparted by exsolved H_2O and CO_2 fluids or reservoir overpressure.

Current surface monitoring demonstrates the modern Yellowstone volcanic system persistently degasses enormous quantities of CO_2 derived from mantle basalts and basement (Werner and Brantley, 2003; Lowenstern and Hurwitz, 2008). The CO_2 flux is sufficient to fully saturate the silicic magma reservoirs at Yellowstone (Lowenstern and Hurwitz, 2008). Modern observations of Yellowstone's changing hydrothermal system and surface deformation may be the response to variations in CO_2 delivery at yearly to decadal timescales. Although speculative, the different ranges of CO_2 dissolved in quartz-hosted melt inclusions from Yellowstone caldera's other rhyolitic eruptions could also reflect pulses of CO_2 flux through the system (e.g., Huckleberry Ridge cupolas Myers et al., 2016, or Central Plateau Member rhyolites Befus and Gardner, 2016). If true, then one such pulse may be preserved in the Mesa Falls quartz, recorded by the shift from relatively H_2O-rich inclusions to H_2O-poor embayments.

Another possible consequence of this process is that unsteady pulses of CO_2 flux may have produced a nonequilibrium, temporarily volatile-undersaturated melt. Nonequilibrium exchange is possible because the diffusivity of CO_2 is roughly one order of magnitude slower than H_2O (Gonnermann and Manga, 2005; Yoshimura and Nakamura, 2011; Yoshimura, 2015). In response to CO_2 flux, H_2O exsolves quickly at the wt.% level, nucleating and growing H_2O-rich bubbles. CO_2 dissolves much more slowly into the melt at the 10s to 100s of ppm. The consequence is a temporarily volatile-undersaturated melt, depleted in H_2O. Steady CO_2 flux will drive the system back to equilibrium solubility as diffusion-limited CO_2 dissolution offsets the kinetic undersaturation caused by rapid H_2O exsolution.

With either equilibrium or nonequilibrium exchange, the CO_2 flux must have been associated with significant heat transfer in order to prevent crystallization caused by the reduced activity of H_2O and possible decompression. Indeed, the elevated K_2O and Ba in embayments exclude crystallization of a mineral assemblage rich in sanidine and might instead indicate crystal dissolution. Sanidine dissolution is not required, however, CO_2 fluids are known to transport alkalis and other metals (Arienzo et al., 2016; Van Hinsberg et al., 2016). In addition, Caricchi et al. (2018) demonstrated assimilation of CO_2 fluids by the Bishop Tuff rhyolite produced higher temperatures and notably increased K_2O in the melt. Our data are equivocal in this regard as some alkalis and metals are enriched in embayments (K_2O) whereas others are not (Na_2O, TiO_2). This minor compositional inconsistency could also be attributed to intrusion and mixing of a drier and hotter rhyolite that accompanied CO_2 flux (Fig. 4). As would be expected with compositionally-similar rhyolites, we find little additional evidence either for or against mixing. Although we cannot definitively isolate the process that produced the change, the volatile, major, and trace element concentrations in the inclusions and embayment interiors clearly represent separate episodes in the reservoir.

The lack of similarity in H_2O content between inclusions and embayment interiors hints at a timescale for the CO_2 flux event prior to eruption. In addition, both faceted and rounded glass inclusions preserve similar H_2O, and neither population preserve bubble or microlite textures that indicate degassing. We thus conclude quartz-hosted inclusions did not lose significant H_2O during eruptive decompression, or in the unknown amount of time preceding it. H_2O loss is well documented in olivine-hosted and clinopyroxene-hosted inclusion studies (Gaetani et al., 2012), but there is no consensus for quartz-hosted rhyolite inclusions. Limited experimental work suggests that H_2O loss may occur in quartz-hosted glass inclusions in >12 hours (Severs et al., 2007), and H^+ can diffuse quickly through quartz (e.g., Jollands et al., 2020). This mechanism has been inferred to reconcile scatter in quartz-hosted glass inclusion H_2O contents (Myers et al., 2016, 2018, 2019; Waelkens et al., 2022). However, slowly cooled quartz-hosted inclusions from lavas, ignimbrites, and experimentally homogenized melt inclusions can preserve original magmatic H_2O contents. At Mesa Falls the H_2O contents of glass inclusions present evidence for little to no modification via post-entrapment H^+ diffusive loss through the quartz host.

4.3. Embayments reveal slow decompression

Volatile concentration gradients are produced via diffusion-limited re-equilibration of melt along the embayments because the embayment melt remains connected to external melt. In the past decades volatile gradients have been documented in embayments from pyroclastic deposits at many silicic and mafic volcanoes (e.g., Anderson, 1991; Liu et al., 2007; Humphreys et al., 2008). Diffusion modeling of those records indicates the gradients are produced by changing conditions in the external melt during decompression. Embayments are now considered a reliable tool to reconstruct eruptive magma ascent rates (e.g., Lloyd et al., 2014; Myers et al., 2016, 2018, 2021; Ferguson et al., 2016; Moussallam et al., 2019; Newcombe et al., 2020; Saalfeld et al., 2022; Geshi et al., 2021). Mesa Falls CO_2 gradients resemble archetypal gradients described in the literature, marked by flat interiors that gradually transition to convex diffusion-limited concentration gradients 150 to 250 µm from the embayment exterior. Because H_2O diffuses ~10x faster than CO_2 we expected H_2O to also preserve distinct, convex concentration gradients that extended further into embayment interiors than CO_2. Instead, the H_2O gradients curve upward from interior plateaus of 0.9±0.1 wt.% to enrichments reaching 2.0 to 2.4 wt.% in the final 10s of microns near the mouth. These enrichments, dominated by molecular H_2O, were generated by post-eruptive secondary rehydration. The rehydration portions of the profiles can thus be disregarded for the purposes of this study, because our focus is on pre- and syn-eruptive processes.

Best fit 1D and 2D diffusion models using embayment interior concentrations as the starting volatile contents match the flat, unaltered interior H_2O contents and the full length of the CO_2 distributions (Fig. 7, Supplemental 4). Models using a ~0.2 wt.% exsolved H_2O-rich fluid fit best, but an exsolved volatile phase up to 2 wt.% also returns satisfactory fits and changes the associated diffusion timescale by <10%. Notably, an initial exsolved fluid phase is consistent with a CO_2 flux event prior to decompression. Higher exsolved fluid contents return H_2O profiles with significant gradients, which is inconsistent with our H_2O data. We report model results using 800 °C, however equally good fits can be produced from 750 to 850 °C. Increasing or decreasing temperature by 50 °C changes the diffusion timescale by ~2x. Quench pressures range from 10 to 43 MPa, in accordance with estimates for fragmentation depths for silicic systems (e.g., Papale et al., 1998). Decompression rate best fits for the 1D profiles range from $10^{-2.8}$ to $10^{-3.9}$ MPa s^{-1}, with a mean of $10^{-3.4\pm0.5}$ MPa s^{-1} (2σ, n=40). The 2D models recover similar decompression timescales ranging from $10^{-2.7}$ to $10^{-3.9}$ MPa s^{-1}, with a mean of $10^{-3.3\pm0.6}$ MPa s^{-1} (2σ, n=15) (Fig. 8, Supplemental 4).

The best fit decompression rates are equivalent to ascent rates ranging from 400 to 7000 m day^{-1} (0.005 to 0.08 m s^{-1}), assuming an overburden density of 2600 kg m^{-3}. The rates derived from diffusive timescales by the Mesa Falls quartz-hosted embayments are as slow or slower than the slowest values calculated using embayments from other Plinian, caldera-forming eruptions (Fig. 8) (Liu et al., 2007; Myers et al., 2018, 2021; Geshi et al., 2021; Saalfeld et al., 2022). They are also slower than estimates for Yellowstone's Huckleberry Ridge Tuff (Myers et al., 2016, 2018). Indeed, Mesa Falls Tuff decompression rates are the slowest retrieved from natural samples by most techniques for explosive silicic eruptions, although some experimental work demonstrate rates less than 10^{-4} MPa s^{-1} are possible (<240 m day^{-1}, or 0.003 m s^{-1}) (Couch et al., 2003; Castro and Gardner, 2008; Cassidy et al., 2018). We suggest that the distribution of H_2O and CO_2 in Mesa Falls embayments represents a fluid-saturated, pre-eruptive magmatic migration to shallower depths before the caldera-forming eruption event. There is no crystal growth or microlite evidence for this migration. For this reason, it may have occurred in the days prior to eruption, or have even been an initial stage of the eruption.

The relatively slow process building towards the final explosive eruption of the Mesa Falls Tuff that we have proposed here is consistent with multi-stage processes inferred by other embayment studies (e.g., Myers et al., 2021; Geshi et al., 2021). Saalfeld et al. (2022), for example, found that melt from the Guaje pumice of Bandelier Tuff equilibrated at shallow pre-eruptive conditions after a prolonged ascent for hours to days prior to final erup-

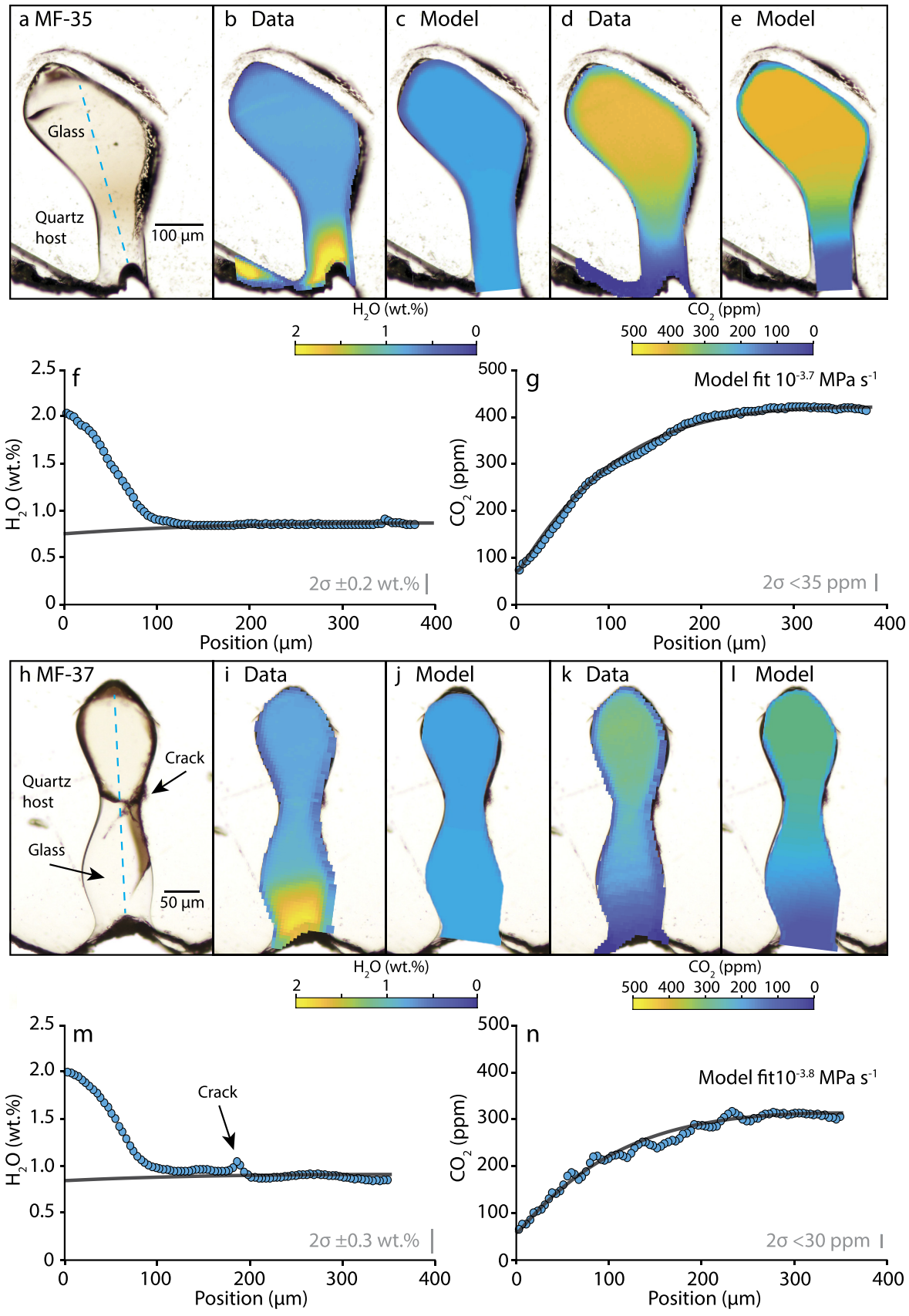

Fig. 7. Measured and modeled distribution of volatiles in embayments MF-35 (a to g) and MF-37 (h to n) along 1D transects shown in blue dashed line and 2D maps. In 1D the blue circles are the measured data and the black line is the best fit model. Gray numbers and bar indicate 2σ uncertainty. Adjacent panels "Data" and "Model" show the best fit to the 2D maps. For both embayments the 1D and 2D models produce consistent decompression rates. As in Fig. 2, position marks increasing distance into the host crystal (f, g, m, n).

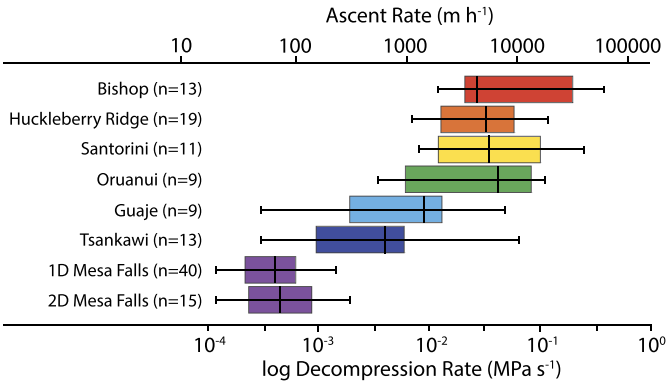

Fig. 8. Decompression rates calculated from Mesa Falls embayments from 1D transects and 2D maps shown in purple. Embayments in the Mesa Falls record slower timescales than those from other silicic systems, with data compiled for Tsankawi and Guaje Bandelier Tuffs from Saalfeld et al. (2022), Oruanui from Myers et al. (2018), Santorini from Myers et al. (2021), Huckleberry Ridge from Myers et al. (2016 and 2018); and Bishop from Myers et al. (2018). Box and whisker plots show central quartiles as the box, the internal line as the mean, and the end lines as the max and min, respectively.

tion. Quartz-hosted embayments from the Guaje pumice, however, record the rapid ascent. The Mesa Falls embayments differ from previous embayment studies because they consistently record the slow pre-eruptive process rather than syn-eruptive ascent. The final eruptive decompression of Mesa Falls was likely too fast to be recorded by volatile diffusion in the embayments. This inference aligns with Li diffusion in plagioclase, which have shown final ascent on the order of tens of minutes for the Mesa Falls Tuff (Neukampf et al., 2021). Similarly, quartz from the Mesa Falls Tuff are depleted in hydrogen at crystal rims and enriched by charge-balancing Li (Neukampf et al., 2022; Tollan et al., 2019). This is consistent with H-Li in quartz speedometry, which has been applied to quartz from the Oruanui and Bishop Tuff, capturing rapid ascent rates on the order of minutes to hours (Charlier et al., 2012; Jollands et al., 2020).

5. Conclusion

Crystals are the record keepers of subsurface processes we cannot see. Quartz-hosted embayments and glass inclusions in the Mesa Falls Tuff (Yellowstone, USA) allow us to reconstruct processes that connect magma storage, migration, and eruption dynamics. Fully enclosed glass inclusions in quartz retain the composition of the magma reservoir during an episode of fractional crystallization of the observed mineral assemblage. Estimates ranging from ~30 to ~60% crystallization align with expectations at Yellowstone caldera. Trace element and K_2O concentrations in embayment interiors are elevated compared to glass inclusions. Embayment interiors are also significantly depleted in H_2O although CO_2 contents are largely similar. The transition to H_2O-poor embayment interiors most likely occurred in response to CO_2 flux event, perhaps accompanied by rhyolite intrusion and mixing. Magmatic CO_2 fluxing should be expected at Yellowstone caldera, which actively degasses vast amounts of CO_2 at the surface each year. Diffusion-limited H_2O and CO_2 distributions along the full length of the embayments preserve a decompression timescale of $\sim 10^{-3.4}$ MPa s^{-1}. Such rates are slower than anticipated for syn-eruptive ascent of rhyolite melt. Instead, the embayments may record the timescale of the magma reservoir breaching into the shallower subsurface prior to the onset of the caldera-forming Mesa Falls eruption.

CRediT authorship contribution statement

Kenneth Befus: Conceptualization, methodology, investigation, resources, writing, funding acquisition.

Anna Ruefer: Methodology, investigation, resources, writing.

Chelsea Allison: Methodology, investigation, resources, software, visualization, writing.

James Thompson: Methodology, investigation, resources, visualization, software, writing.

Declaration of competing interest

The authors declare that they have no known competing financial interests or personal relationships that could have appeared to influence the work reported in this paper.

Data availability

Data and codes are provided within the document and supplemental package.

Acknowledgements

We thank Nathan Miller and Andrew Mott for operating and processing the LA-ICP-MS and electron microprobe data, respectively. We also thank Ben Black and Ben Andrews for their discussions on diffusion modeling. Two anonymous reviewers improved the manuscript. This research was made possible by a grant from the National Science Foundation to KB (grant EAR 2015255). This research used resources of the Advanced Light Source, a U.S. DOE Office of Science User Facility under contract no. DE-AC02-05CH11231.

Appendix A. Supplementary material

Supplementary material related to this article can be found online at https://doi.org/10.1016/j.epsl.2022.117909.

References

Anderson Jr, A.T., Newman, S., Williams, S.N., Druitt, T.H., Skirius, C., Stolper, E., 1989. H_2O, CO_2, Cl, and gas in Plinian and ash-flow Bishop rhyolite. Geology 17 (3), 221–225.

Anderson, A.T., 1991. Hourglass inclusions: theory and application to the Bishop Rhyolitic Tuff. Am. Mineral. 76 (3–4), 530–547.

Arienzo, I., Mazzeo, F.C., Moretti, R., Cavallo, A., D'Antonio, M., 2016. Open-system magma evolution and fluid transfer at Campi Flegrei caldera (Southern Italy) during the past 5 ka as revealed by geochemical and isotopic data: the example of the Nisida eruption. Chem. Geol. 427, 109–124.

Bachmann, O., Wallace, P.J., Bourquin, J., 2010. The melt inclusion record from the rhyolitic Kos Plateau Tuff (Aegean Arc). Contrib. Mineral. Petrol. 159 (2), 187–202.

Befus, K.S., Gardner, J.E., 2016. Magma storage and evolution of the most recent effusive and explosive eruptions from Yellowstone Caldera. Contrib. Mineral. Petrol. 171 (4), 1–19.

Behrens, H., Tamic, N., Holtz, F., 2004. Determination of the molar absorption coefficient for the infrared absorption band of CO_2 in rhyolitic glasses. Am. Mineral. 89 (2–3), 301–306.

Bindeman, I.N., Valley, J.W., 2001. Low-$\delta^{18}O$ rhyolites from Yellowstone: magmatic evolution based on analyses of zircons and individual phenocrysts. J. Petrol. 42 (8), 1491–1517.

Blundy, J., Cashman, K.V., Rust, A., Witham, F., 2010. A case for CO_2-rich arc magmas. Earth Planet. Sci. Lett. 290 (3–4), 289–301.

Brugman, K., Till, C.B., Bose, M., 2022. Common assumptions and methods yield overestimated diffusive timescales, as exemplified in a Yellowstone post-caldera lava. Contrib. Mineral. Petrol. 177 (6), 1–19.

Caricchi, L., Sheldrake, T.E., Blundy, J., 2018. Modulation of magmatic processes by CO_2 flushing. Earth Planet. Sci. Lett. 491, 160–171.

Cassidy, M., Manga, M., Cashman, K., Bachmann, O., 2018. Controls on explosive-effusive volcanic eruption styles. Nat. Commun. 9 (1), 1–16.

Castro, J.M., Gardner, J.E., 2008. Did magma ascent rate control the explosive-effusive transition at the Inyo volcanic chain, California? Geology 36 (4), 279–282.

Charlier, B.L.A., Morgan, D.J., Wilson, C.J.N., Wooden, J.L., Allan, A.S.R., Baker, J.A., 2012. Lithium concentration gradients in feldspar and quartz record the final minutes of magma ascent in an explosive supereruption. Earth Planet. Sci. Lett. 319, 218–227.
Christiansen, R.L., 2001. The Quaternary and Pliocene Yellowstone Plateau Volcanic Field of Wyoming, Idaho, and Montana, vol. 729. US Department of the Interior, US Geological Survey.
Couch, S., Sparks, R.S.J., Carroll, M.R., 2003. The kinetics of degassing-induced crystallization at Soufriere Hills Volcano, Montserrat. J. Petrol. 44 (8), 1477–1502.
deGraffenried, R.L., Shea, T., 2021. Using volatile element concentration profiles in crystal-hosted melt embayments to estimate magma decompression rate: assumptions and inherited errors. Geochem. Geophys. Geosyst. 22 (5), e2021GC009672.
Edmonds, M., Woods, A.W., 2018. Exsolved volatiles in magma reservoirs. J. Volcanol. Geotherm. Res. 368, 13–30.
Ellis, B.S., Mark, D.F., Troch, J., Bachmann, O., Guillong, M., Kent, A.J., von Quadt, A., 2017. Split-grain $^{40}Ar/^{39}Ar$ dating: integrating temporal and geochemical data from crystal cargoes. Chem. Geol. 457, 15–23.
Ferguson, D.J., Gonnermann, H.M., Ruprecht, P., Plank, T., Hauri, E.H., Houghton, B.F., Swanson, D.A., 2016. Magma decompression rates during explosive eruptions of Kīlauea volcano, Hawaii, recorded by melt embayments. Bull. Volcanol. 78 (10), 1–12.
Gaetani, G.A., O'Leary, J.A., Shimizu, N., Bucholz, C.E., Newville, M., 2012. Rapid reequilibration of H_2O and oxygen fugacity in olivine-hosted melt inclusions. Geology 40 (10), 915–918.
Georgeais, G., Koga, K.T., Moussallam, Y., Rose-Koga, E.F., 2021. Magma decompression rate calculations with EMBER: a user-friendly software to model diffusion of H_2O, CO_2, and S in melt embayments. Geochem. Geophys. Geosyst. 22 (7), e2020GC009542.
Geshi, N., Yamasaki, T., Miyagi, I., Conway, C.E., 2021. Magma chamber decompression during explosive caldera-forming eruption of Aira caldera. Commun. Earth Environ. 2 (1), 1–10.
Gonnermann, H.M., Manga, M., 2005. Nonequilibrium magma degassing: results from modeling of the ca. 1340 AD eruption of Mono Craters, California. Earth Planet. Sci. Lett. 238 (1–2), 1–16.
Gualda, G.A., Ghiorso, M.S., Lemons, R.V., Carley, T.L., 2012. Rhyolite-MELTS: a modified calibration of MELTS optimized for silica-rich, fluid-bearing magmatic systems. J. Petrol. 53 (5), 875–890.
Humphreys, M.C., Menand, T., Blundy, J.D., Klimm, K., 2008. Magma ascent rates in explosive eruptions: constraints from H_2O diffusion in melt inclusions. Earth Planet. Sci. Lett. 270 (1–2), 25–40.
Jollands, M.C., Ellis, B., Tollan, P.M., Müntener, O., 2020. An eruption chronometer based on experimentally determined H-Li and H-Na diffusion in quartz applied to the Bishop Tuff. Earth Planet. Sci. Lett. 551, 116560.
Leeman, W.P., Phelps, D.W., 1981. Partitioning of rare earths and other trace elements between sanidine and coexisting volcanic glass. J. Geophys. Res., Solid Earth 86 (B11), 10193–10199.
Liu, Y., Zhang, Y., Behrens, H., 2005. Solubility of H_2O in rhyolitic melts at low pressures and a new empirical model for mixed H_2O–CO_2 solubility in rhyolitic melts. J. Volcanol. Geotherm. Res. 143 (1–3), 219–235.
Liu, Y., Anderson, A.T., Wilson, C.J., 2007. Melt pockets in phenocrysts and decompression rates of silicic magmas before fragmentation. J. Geophys. Res., Solid Earth 112 (B6).
Lloyd, A.S., Ruprecht, P., Hauri, E.H., Rose, W., Gonnermann, H.M., Plank, T., 2014. NanoSIMS results from olivine-hosted melt embayments: magma ascent rate during explosive basaltic eruptions. J. Volcanol. Geotherm. Res. 283, 1–18.
Lowenstern, J.B., 1995. Applications of silicate-melt inclusions to the study of magmatic volatiles. In: Magmas, Fluids and Ore Deposits, vol. 23, pp. 71–99.
Lowenstern, J.B., Hurwitz, S., 2008. Monitoring a supervolcano in repose: heat and volatile flux at the Yellowstone Caldera. Elements 4 (1), 35–40.
McIntosh, I.M., Nichols, A.R., Tani, K., Llewellin, E.W., 2017. Accounting for the species-dependence of the 3500 cm^{-1} H_2Ot infrared molar absorptivity coefficient: implications for hydrated volcanic glasses. Am. Mineral. 102 (8), 1677–1689.
Moussallam, Y., Rose-Koga, E.F., Koga, K.T., Médard, E., Bani, P., Devidal, J.L., Tari, D., 2019. Fast ascent rate during the 2017–2018 Plinian eruption of Ambae (Aoba) volcano: a petrological investigation. Contrib. Mineral. Petrol. 174 (11), 1–24.
Myers, M.L., Wallace, P.J., Wilson, C.J., Morter, B.K., Swallow, E.J., 2016. Prolonged ascent and episodic venting of discrete magma batches at the onset of the Huckleberry Ridge supereruption, Yellowstone. Earth Planet. Sci. Lett. 451, 285–297.
Myers, M.L., Wallace, P.J., Wilson, C.J., Watkins, J.M., Liu, Y., 2018. Ascent rates of rhyolitic magma at the onset of three caldera-forming eruptions. Am. Mineral. 103 (6), 952–965.
Myers, M.L., Wallace, P.J., Wilson, C.J., 2019. Inferring magma ascent timescales and reconstructing conduit processes in explosive rhyolitic eruptions using diffusive losses of hydrogen from melt inclusions. J. Volcanol. Geotherm. Res. 369, 95–112.
Myers, M.L., Druitt, T.H., Schiavi, F., Gurioli, L., Flaherty, T., 2021. Evolution of magma decompression and discharge during a Plinian event (Late Bronze-Age eruption, Santorini) from multiple eruption-intensity proxies. Bull. Volcanol. 83 (3), 1–17.
Neace, T.F., Hackett, W.R., Davis, L.C., Johnson, R.J., Link, P.K., 1986. Eruptive style, emplacement, and lateral variations of the Quaternary Mesa Falls Tuff. Island Park, Idaho.
Neukampf, J., Ellis, B.S., Magna, T., Laurent, O., Bachmann, O., 2019. Partitioning and isotopic fractionation of lithium in mineral phases of hot, dry rhyolites: the case of the Mesa Falls Tuff, Yellowstone. Chem. Geol. 506, 175–186.
Neukampf, J., Ellis, B.S., Laurent, O., Steinmann, L.K., Ubide, T., Oeser, M., et al., Bachmann, O., 2021. Time scales of syneruptive volatile loss in silicic magmas quantified by Li isotopes. Geology 49 (2), 125–129.
Neukampf, J., Laurent, O., Tollan, P., Bouvier, A.S., Magna, T., Ulmer, P., et al., Bachmann, O., 2022. Degassing from magma reservoir to eruption in silicic systems: the Li elemental and isotopic record from rhyolitic melt inclusions and host quartz in a Yellowstone rhyolite. Geochim. Cosmochim. Acta 326, 56–76.
Newcombe, M.E., Plank, T., Barth, A., Asimow, P.D., Hauri, E., 2020. Water-in-olivine magma ascent chronometry: every crystal is a clock. J. Volcanol. Geotherm. Res. 398, 106872.
Newman, S., Stolper, E.M., Epstein, S., 1986. Measurement of water in rhyolitic glasses; calibration of an infrared spectroscopic technique. Am. Mineral. 71 (11–12), 1527–1541.
Ni, H., Zhang, Y., 2008. H_2O diffusion models in rhyolitic melt with new high pressure data. Chem. Geol. 250 (1–4), 68–78.
Pamukcu, A.S., Gualda, G.A., Bégué, F., Gravley, D.M., 2015. Melt inclusion shapes: timekeepers of short-lived giant magma bodies. Geology 43 (11), 947–950.
Papale, P., Neri, A., Macedonio, G., 1998. The role of magma composition and water content in explosive eruptions: 1. Conduit ascent dynamics. J. Volcanol. Geotherm. Res. 87 (1–4), 75–93.
Pappalardo, L., Buono, G., Fanara, S., Yi, J., Shan, X., Guo, Z., et al., Ventura, G., 2022. The role of CO_2 flushing in triggering the 'Millennium'eruption and recent unrests at Changbaishan volcano (China/North Korea). Int. Geol. Rev., 1–14.
Rivera, T.A., Schmitz, M.D., Jicha, B.R., Crowley, J.L., 2016. Zircon petrochronology and $^{40}Ar/^{39}Ar$ sanidine dates for the Mesa Falls Tuff: crystal-scale records of magmatic evolution and the short lifespan of a large Yellowstone magma chamber. J. Petrol. 57 (9), 1677–1704.
Ruefer, A.C., Befus, K.S., Thompson, J.O., Andrews, B.J., 2021. Implications of multiple disequilibrium textures in quartz-hosted embayments. Front. Earth Sci. 9, 742895.
Saalfeld, M.A., Myers, M.L., deGraffenried, R., Shea, T., Waelkens, C.M., 2022. On the rise: using reentrants to extract magma ascent rates in the Bandelier Tuff caldera complex, New Mexico, USA. Bull. Volcanol. 84 (1), 1–21.
Severs, M.J., Azbej, T., Thomas, J.B., Mandeville, C.W., Bodnar, R.J., 2007. Experimental determination of H_2O loss from melt inclusions during laboratory heating: evidence from Raman spectroscopy. Chem. Geol. 237 (3–4), 358–371.
Spilliaert, N., Allard, P., Métrich, N., Sobolev, A.V., 2006. Melt inclusion record of the conditions of ascent, degassing, and extrusion of volatile-rich alkali basalt during the powerful 2002 flank eruption of Mount Etna (Italy). J. Geophys. Res., Solid Earth 111 (B4).
Stelten, M.E., Cooper, K.M., Vazquez, J.A., Calvert, A.T., Glessner, J.J., 2015. Mechanisms and timescales of generating eruptible rhyolitic magmas at Yellowstone caldera from zircon and sanidine geochronology and geochemistry. J. Petrol. 56 (8), 1607–1642.
Stelten, M.E., Champion, D.E., Kuntz, M.A., 2018. The timing and origin of pre- and post-caldera volcanism associated with the Mesa Falls Tuff, Yellowstone Plateau volcanic field. J. Volcanol. Geotherm. Res. 350, 47–60.
Tollan, P., Ellis, B., Troch, J., Neukampf, J., 2019. Assessing magmatic volatile equilibria through FTIR spectroscopy of unexposed melt inclusions and their host quartz: a new technique and application to the Mesa Falls Tuff, Yellowstone. Contrib. Mineral. Petrol. 174 (3), 1–19.
Troch, J., Ellis, B.S., Schmitt, A.K., Bouvier, A.S., Bachmann, O., 2018. The dark side of zircon: textural, age, oxygen isotopic and trace element evidence of fluid saturation in the subvolcanic reservoir of the Island Park-Mount Jackson Rhyolite, Yellowstone (USA). Contrib. Mineral. Petrol. 173 (7), 1–17.
Van Hinsberg, V.J., Berlo, K., Migdisov, A.A., Williams-Jones, A.E., 2016. CO_2-fluxing collapses metal mobility in magmatic vapour. Geochem. Perspect. Lett. 824 (LA-UR-15-28200).
Vazquez, J.A., Reid, M.R., 2002. Time scales of magma storage and differentiation of voluminous high-silica rhyolites at Yellowstone caldera, Wyoming. Contrib. Mineral. Petrol. 144 (3), 274–285.
Vazquez, J.A., Stelten, M.E., Bindeman, I.N., Cooper, K., 2017. A field trip guide to the petrology of Quaternary volcanism on the Yellowstone Plateau (No. 2017-5022-Q). US Geological Survey.
Waelkens, C.M., Stix, J., Eves, E., Gonzalez, C., Martineau, D., 2022. H_2O and CO_2 evolution in the Bandelier Tuff sequence reveals multiple and discrete magma replenishments. Contrib. Mineral. Petrol. 177 (1), 1–23.
Wallace, P.J., Anderson, A.T., Davis, A.M., 1995. Quantification of pre-eruptive exsolved gas contents in silicic magmas. Nature 377 (6550), 612–616.
Watts, K.E., Bindeman, I.N., Schmitt, A.K., 2012. Crystal scale anatomy of a dying supervolcano: an isotope and geochronology study of individual phenocrysts from voluminous rhyolites of the Yellowstone caldera. Contrib. Mineral. Petrol. 164 (1), 45–67.

Werner, C., Brantley, S., 2003. CO_2 emissions from the Yellowstone volcanic system. Geochem. Geophys. Geosyst. 4 (7).
Yoshimura, S., Nakamura, M., 2011. Carbon dioxide transport in crustal magmatic systems. Earth Planet. Sci. Lett. 307 (3–4), 470–478.
Yoshimura, S., 2015. Diffusive fractionation of H_2O and CO_2 during magma degassing. Chem. Geol. 411, 172–181.
Zhang, Y., Belcher, R., Ihinger, P.D., Wang, L., Xu, Z., Newman, S., 1997. New calibration of infrared measurement of dissolved water in rhyolitic glasses. Geochim. Cosmochim. Acta 61 (15), 3089–3100.
Zhang, Y., Ni, H., 2010. Diffusion of H, C, and O components in silicate melts. Rev. Mineral. Geochem. 72 (1), 171–225.